Computer Assisted Mechanics and Engineering Sciences, 13: 669–682, 2006.

Finite element analysis of fluid influence on instabilities in two-phase Cam-clay plasticity model

Anna Stankiewicz, Jerzy Pamin
Cracow University of Technology, Institute for Computational Civil Engineering
ul. Warszawska 24, 31-155 Cracow, Poland

(Received in the final form October 31, 2006)

The influence of fluid phase on soil instabilities is investigated using the modified Cam-clay model within a two-phase description. Spurious mesh dependence of finite element results is prevented by a gradient enhancement of the model. The results of numerical tests for one-phase and two-phase model are compared. The influence of permeability on the stabilizing role of the fluid phase is assessed.

Keywords: two-phase medium, finite element method, plasticity, Cam-clay model, gradient regularization, localization

1. Introduction

The solid–fluid interaction influences the critical load level for which an instability can occur as well as the direction and width of the localized deformation bands. In particular, the permeability coefficient and the pore fluid compressibility are found to affect localization. However, it is unclear whether its onset of instability in a two-phase medium coincides with that in the underlying drained solid, cf. for instance [1, 10]. In this paper the influence of fluid phase on soil instabilities is investigated using the local and gradient-enhanced modified Cam-clay model.

In [1] an investigation of the plane-strain instability of saturated porous media is performed. It is concluded that the elastic-plastic models can exhibit two-phase instability despite the fact that the solid phase remains in the stable regime. The contractant hardening materials are found to be more inclined to two-phase instability than dilatant ones. In [10], the problem of strain localization in porous materials is thoroughly discussed. The author confirms that the localized solution is possible when the acoustic tensor associated with the underlying drained material becomes singular. It is concluded that soil under undrained conditions requires stronger softening than drained soil in order to reach a state where localization is possible.

Moreover, in [17] it is claimed that the two-phase modelling of soil involves a certain regularization by introducing a gradient term via the Darcy's law, although the necessity of regularization of the constitutive model for a multiphase material is usually recognized. In [20] a gradient plasticity model is used to analyze dynamic instabilities in fully and partially saturated granular material. The influence of permeability on the width of localization zone in a one-dimensional test is also evaluated. In [13] a gradient-enhanced visco-plastic model is applied to localization analysis of clays. In [2] it is shown that the length scale introduced by incorporating the fluid flow depends on the integration time step and thus is insufficient for the regularization of unstable behaviour.

More recent developments concerning the problem of numerical simulations of localized deformation bands in multiphase (granular) media are covered for instance in [3, 5, 11, 14, 21]. In this paper attention is limited to static two-phase modelling and small deformations. In [3] the problem of deformation and strain localization in partially saturated porous medium is considered and a constitutive model (extension of modified Cam-clay model) for such a three-phase medium is proposed.

In [14] a general variational framework of Cam-clay theory is built within the finite-deformation plasticity. In [21] the issue of internal length scale introduced by the fluid-solid interaction is considered in a dynamic context. Using stability and dispersion analyses the limit wave numbers are evaluated, for which the internal length parameter vanishes and hence regularization is mandatory. These results are confirmed in [5]. On the other hand, in [11] arguments are given to support the opinion that, at least for saturated sand undergoing dilatation, the fluid phase stabilizes the soil and regularizes the solution.

The present article is organized as follows. Section 2 presents the equations for two-phase modelling of fully saturated soil. In Section 3 we briefly recapitulate the gradient-dependent Cam-clay plasticity theory [18]. Section 4 contains the description of the formulated three-field finite element model, including its linearization and discretization. In Section 5 the evolution of total and effective stresses is compared. The investigation of the effect of the fluid phase on localization phenomena in the local and gradient-enhanced Cam-clay model is carried out using a typical benchmark configuration: plane strain biaxial compression test. Section 6 covers the results of the test showing discretization sensitivity. The influence of model parameters on the instability and localization problem is investigated. Calculations are performed using the development version of the FEAP finite element package. Final remarks are gathered in Section 7.

2. TWO-PHASE MODELLING

The structure of soil is very complex. It is a multiphase material which consists of a solid skeleton and voids partly occupied by water and air (partially saturated soil). The interactions of the phases strongly affect the properties and behaviour of soils.

In the present paper we limit our investigation to the important case when soil pores are completely filled with water, i.e. when soil is fully saturated and can be treated as a two-phase material. Then, the fundamental problem variables are: solid displacement vector and water pore pressure. Such a two-phase medium, with the assumption of incompressibility of solid grains, is governed by the following two equations valid in the considered volume Ω, cf. for instance [19, 22],

$$\boldsymbol{L}^{\mathrm{T}}\boldsymbol{\sigma}_t + \hat{\rho}\boldsymbol{g} = \boldsymbol{0}, \tag{1}$$

$$\boldsymbol{\nabla}\cdot\dot{\boldsymbol{u}} + \boldsymbol{\nabla}\cdot\boldsymbol{v}_d + n\frac{\dot{p}_f}{K_f} = 0, \tag{2}$$

with

$$\boldsymbol{\sigma_t} = \boldsymbol{\sigma} - \boldsymbol{\Pi}\, p_f\,, \qquad \hat{\rho} = (1-n)\rho_s + n\rho_f\,, \tag{3}$$

and Darcy's fluid flow velocity given by

$$\boldsymbol{v}_d = -\boldsymbol{k}\boldsymbol{\nabla}\left(\frac{p_f}{\gamma_f} + z\right). \tag{4}$$

In Eqs. (1)–(4), $\boldsymbol{L}$ is the differential operator matrix (Voigt's notation is used), $\boldsymbol{\sigma}_t$ is the total stress tensor, $\hat{\rho}$ – saturated density of the soil-fluid mixture, $\boldsymbol{g}$ – gravitation vector, $\boldsymbol{u}$ – displacement vector, n – porosity, p_f is the excess pore pressure, K_f – fluid bulk modulus, $\boldsymbol{\sigma}$ is the effective stress tensor, $\boldsymbol{\Pi} = [1,1,1,0,0,0]^T$, ρ_s – density of the solid phase, ρ_f – density of the fluid phase, $\boldsymbol{k}$ – permeability matrix, $\gamma_f = \rho_f g$, and z – coordinate in the direction of gravitation, governing the stationary state of pore pressure. The porosity n and void ratio e are related by: $n = e/(1+e)$. The adopted sign convention is that the compressive pressure is regarded as positive. Equation (1) represents the balance of momentum and Eq. (2) the balance of mass. They require appropriate boundary and initial conditions.

The initial conditions for displacements and pore pressures at time $t = 0$ are

$$\boldsymbol{u} = \boldsymbol{u}_0\,, \qquad p_f = p_{f0}\,. \tag{5}$$

The boundary conditions to be satisfied at any time t are

$$\boldsymbol{\sigma}_t\boldsymbol{\nu} = \bar{\boldsymbol{t}} \quad \text{on } \Gamma_t\,, \qquad \boldsymbol{v}_d\boldsymbol{\nu} = \bar{\boldsymbol{q}} \quad \text{on } \Gamma_q\,, \qquad \boldsymbol{u} = \bar{\boldsymbol{u}} \quad \text{on } \Gamma_u\,, \qquad p_f = \bar{p}_f \quad \text{on } \Gamma_p\,, \tag{6}$$

where $\boldsymbol{\nu}$ is the normal to the boundary and $\Gamma_t, \ldots, \Gamma_p$ are appropriate boundary parts.

3. Modified gradient-dependent Cam-clay model

The modified Cam-clay model originated in [16] is commonly accepted as reliable for cohesive soils. It belongs to critical state models [8] and describes the behaviour of the soil skeleton, since the constitutive equations are written in terms of effective stresses. This plastic model, combined with nonlinear elasticity, is capable of reproducing the essential physical properties of soils, including hardening/softening and contraction/dilatation.

The dilatant (softening) and possibly also non-associative response of the Cam-clay model implies the necessity of regularization in order to avoid the loss of ellipticity of the governing equations and to stabilize the numerical response. Although alternative regularization methods, i.e. a rate-dependent (e.g. visco-plastic), micro-polar or nonlocal integral formulation could prove equally effective, cf. for instance [4], or even simpler in terms of implementation, a gradient enhancement of the model is employed due to its generality.

In this regularization concept, higher-order spatial gradients of different components of the constitutive model can be incorporated. If isotropy is assumed, the Laplacian is an optimal regularizing operator. Here, as in [6, 7, 12], it is proposed to make the Cam-clay yield function dependent on the Laplacian of plastic multiplier Λ [18]. The yield condition $f = 0$ then becomes a differential equation which must be solved numerically in addition to the momentum balance equations. This is achieved by taking the weak form of the yield condition, which means it is not imposed pointwise, but in an integral sense, as was first proposed in [15]. The plastic multiplier is then discretized next to displacements.

Volumetric-deviatoric decomposition is adopted in the formulation and the flow rule is derived from the yield function in the classical associative manner, cf. [9]. The yield function for the gradient-dependent modified Cam-clay model is written as [18]

$$f(\boldsymbol{\sigma}, \Lambda, \nabla^2\Lambda) = q^2 + M^2 p\,[p - p_c(\Delta\theta^{\mathrm{p}}) + c\nabla^2\Lambda], \tag{7}$$

where the equivalent deviatoric stress q is defined as $q = \sqrt{3J_2}$, M is a function of the internal friction angle ϕ: $M = \frac{6\sin\phi}{3-\sin\phi}$, p is the effective pressure acting on the soil skeleton, which is assumed to evolve according to the following secant relation [9],

$$p(\Delta\theta^{\mathrm{e}}) = p_0 \exp\left[-\frac{1+e_0}{\kappa}\Delta\theta^{\mathrm{e}}\right], \tag{8}$$

where e_0 denotes the initial void ratio, κ is a positive parameter (called swelling index) which defines the inclination of the unloading and reloading line (Fig. 1), θ^{e} is the volumetric part of the elastic strain tensor. Finally, c is a positive gradient influence factor. In Fig. 1 the local Cam-clay plasticity function (c equal to zero) is plotted.

Further, p_c is the current preconsolidation pressure, the evolution of which is given by a formula similar to Eq. (8),

$$p_c(\Delta\theta^{\mathrm{e}}) = p_{c0} \exp\left[-\frac{1+e_0}{\lambda-\kappa}\Delta\theta^{\mathrm{p}}\right], \tag{9}$$

where λ is the inclination of the virgin consolidation line (Fig. 1), θ^{p} is the volumetric part of the plastic strain tensor, dependent on the plastic multiplier Λ. The details of the formulation can be found in [18], including a discussion of other possible variants of gradient-enhancement of the model.

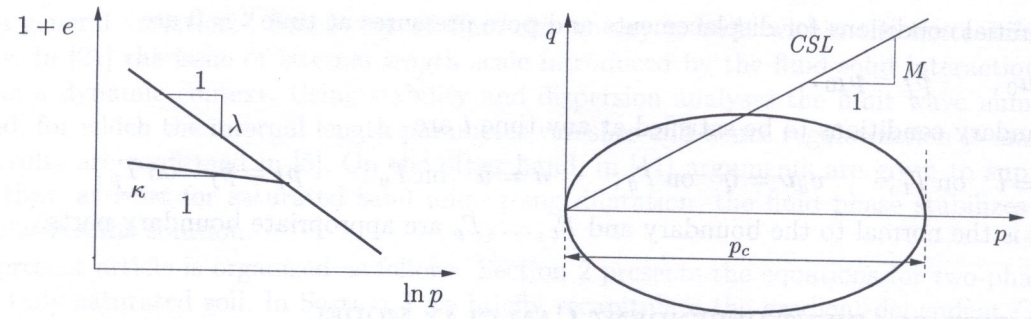

Fig. 1. Material model: elastic behaviour (left) and yield surface (right); CSL denotes the critical state line

4. Discretization of three-field formulation

To discretize the problem of pore pressure evolution combined with the gradient-enhanced plasticity modelling of the solid skeleton, the weak forms of Eqs. (1), (2) and (7) are required.

The weak form of the momentum balance equation reads

$$\int_\Omega \boldsymbol{v}^{\mathrm{T}}(\boldsymbol{\nabla}\boldsymbol{\sigma}_t + \hat{\rho}\boldsymbol{g})\,\mathrm{d}\Omega = \boldsymbol{0}. \tag{10}$$

The weak form of the plastic consistency condition is written as

$$\int_\Omega v_p\, f(\boldsymbol{\sigma}, \Lambda, \nabla^2\Lambda)\,\mathrm{d}\Omega = 0. \tag{11}$$

The weak form of the mass balance equation is

$$\int_\Omega w\left(\boldsymbol{\nabla}\cdot\dot{\boldsymbol{u}} + \boldsymbol{\nabla}\cdot\boldsymbol{v}_d + n\frac{\dot{p}_f}{K_f}\right)\mathrm{d}\Omega = 0. \tag{12}$$

In Eqs. (10)–(12) $\boldsymbol{v}$, v_p and w are suitable weighting functions.

After the integration of momentum and mass balance equations by parts we obtain

$$\int_\Omega (\boldsymbol{L}\boldsymbol{v})^{\mathrm{T}}\boldsymbol{\sigma}_t\,\mathrm{d}\Omega - \int_\Omega \boldsymbol{v}^{\mathrm{T}}\hat{\rho}\boldsymbol{g}\,\mathrm{d}\Omega - \int_{\Gamma_t} \boldsymbol{v}^{\mathrm{T}}\,\bar{\boldsymbol{t}}\,\mathrm{d}\Gamma \qquad = \boldsymbol{0}, \tag{13}$$

$$\int_\Omega w\boldsymbol{\nabla}^{\mathrm{T}}\dot{\boldsymbol{u}}\,\mathrm{d}\Omega - \int_\Omega (\boldsymbol{\nabla}w)^{\mathrm{T}}\boldsymbol{v}_d\,\mathrm{d}\Omega + \int_\Omega w\,\frac{n}{K_f}\,\dot{p}_f\,\mathrm{d}\Omega + \int_{\Gamma_q} w\,\bar{\boldsymbol{q}}\,\mathrm{d}\Gamma_q = 0. \tag{14}$$

In Eqs. (13)–(14) natural boundary conditions have been incorporated.

We introduce the following finite element discretization for displacements $\boldsymbol{u}$, plastic multiplier Λ and excess pore pressure p_f,

$$\boldsymbol{u} = \boldsymbol{N}\boldsymbol{u}^h, \qquad \Lambda = \boldsymbol{h}^{\mathrm{T}}\boldsymbol{\Lambda}^h, \qquad p_f = \boldsymbol{N}_p\boldsymbol{p}^h, \tag{15}$$

where $\boldsymbol{N}$, $\boldsymbol{h}$ and $\boldsymbol{N}_p$ contain the respective interpolation polynomials and $\boldsymbol{u}^h$, $\boldsymbol{\Lambda}^h$ and $\boldsymbol{p}^h$ are vectors with the discrete nodal values. The weighting functions are interpolated similarly according to the Galerkin approach. The used interpolation functions are quadratic for the displacements, linear for the pore pressure and cubic (Hermitean) for the plastic multiplier.

Due to the assumption of linear kinematic relations we can introduce matrix $\boldsymbol{B} = \boldsymbol{L}\boldsymbol{N}$. With vector $\boldsymbol{s} = \nabla^2\boldsymbol{h}$ the discretization of strains and of the Laplacian of plastic multiplier can be expressed as:

$$\boldsymbol{\epsilon} = \boldsymbol{B}\boldsymbol{u}^h, \qquad \nabla^2\Lambda = \boldsymbol{s}^{\mathrm{T}}\boldsymbol{\Lambda}^h. \tag{16}$$

After linearization of the governing equations and after time integration (the implicit backward Euler integration scheme is used) of Eqs. (10) and (14), introducing the employed interpolation of

the problem variables and invoking the usual argument that the weighting functions are arbitrary, the following coupled system of linearized equations in a matrix form is obtained,

$$\begin{bmatrix} \boldsymbol{K}_{uu} & \boldsymbol{K}_{u\Lambda} & -\boldsymbol{K}_{up} \\ \boldsymbol{K}_{\Lambda u} & \boldsymbol{K}_{\Lambda\Lambda} & \boldsymbol{0} \\ \boldsymbol{K}_{up}^{\mathrm{T}} & \boldsymbol{0} & \boldsymbol{K}_{pp} \end{bmatrix} \begin{bmatrix} \Delta \boldsymbol{u}^h \\ \Delta \boldsymbol{\Lambda}^h \\ \Delta \boldsymbol{p}^h \end{bmatrix} = \begin{bmatrix} \boldsymbol{f}_{\mathrm{e}} - \boldsymbol{f}_{\mathrm{i}} \\ \boldsymbol{f}_{\Lambda} \\ \Delta t \Delta \boldsymbol{f}_f \end{bmatrix}. \tag{17}$$

The definitions of the submatrices are as follows,

$$\boldsymbol{K}_{uu} = \int_{\Omega} \boldsymbol{B}^{\mathrm{T}} \frac{\mathrm{d}\boldsymbol{\sigma}}{\mathrm{d}\boldsymbol{\epsilon}} \boldsymbol{B} \, \mathrm{d}\Omega, \tag{18a}$$

$$\boldsymbol{K}_{u\Lambda} = -\int_{\Omega} \boldsymbol{B}^{\mathrm{T}} \frac{\mathrm{d}\boldsymbol{\sigma}}{\mathrm{d}\Lambda} \boldsymbol{h}^{\mathrm{T}} \, \mathrm{d}\Omega, \tag{18b}$$

$$\boldsymbol{K}_{\Lambda u} = -\int_{\Omega} \boldsymbol{h} \frac{\partial f}{\partial \boldsymbol{\sigma}} \frac{\mathrm{d}\boldsymbol{\sigma}}{\mathrm{d}\boldsymbol{\epsilon}} \boldsymbol{B} \, \mathrm{d}\Omega, \tag{18c}$$

$$\boldsymbol{K}_{\Lambda\Lambda} = -\int_{\Omega} \left[\left(\frac{\partial f}{\partial \boldsymbol{\sigma}} \frac{\mathrm{d}\boldsymbol{\sigma}}{\mathrm{d}\Lambda} + \frac{\partial f}{\partial \Lambda} \right) \boldsymbol{h}\boldsymbol{h}^{\mathrm{T}} + \frac{\partial f}{\partial \nabla^2 \Lambda} \boldsymbol{h}\boldsymbol{s}^{\mathrm{T}} \right] \mathrm{d}\Omega, \tag{18d}$$

$$\boldsymbol{K}_{up} = \int_{\Omega} \boldsymbol{B}^{\mathrm{T}} \boldsymbol{\Pi} \boldsymbol{N}_p \, \mathrm{d}\Omega, \tag{18e}$$

$$\boldsymbol{K}_{pp} = \frac{\Delta t}{\gamma_f} \boldsymbol{H} + \boldsymbol{M}, \tag{18f}$$

$$\boldsymbol{H} = \int_{\Omega} (\boldsymbol{\nabla} \boldsymbol{N}_p)^{\mathrm{T}} \boldsymbol{k} \boldsymbol{\nabla} \boldsymbol{N}_p \, \mathrm{d}\Omega, \tag{18g}$$

$$\boldsymbol{M} = \int_{\Omega} \boldsymbol{N}_p^{\mathrm{T}} \frac{n}{K_f} \boldsymbol{N}_p \, \mathrm{d}\Omega, \tag{18h}$$

$$\boldsymbol{f}_{\mathrm{e}} = \int_{\Omega} \boldsymbol{N}^{\mathrm{T}} \hat{\rho} \boldsymbol{g} \, \mathrm{d}\Omega + \int_{\Gamma_t} \boldsymbol{N}^{\mathrm{T}} \bar{\boldsymbol{t}} \, \mathrm{d}\Gamma, \tag{18i}$$

$$\boldsymbol{f}_{\mathrm{i}} = \int_{\Omega} \left(\boldsymbol{B}^{\mathrm{T}} \boldsymbol{\sigma} - \boldsymbol{B}^{\mathrm{T}} \boldsymbol{\Pi} p_f \right) \mathrm{d}\Omega, \tag{18j}$$

$$\boldsymbol{f}_{\Lambda} = \int_{\Omega} \boldsymbol{h} f \left(\boldsymbol{\sigma}, \Lambda, \nabla^2 \Lambda \right) \mathrm{d}\Omega, \tag{18k}$$

$$\boldsymbol{f}_f = \Delta t \left(-\int_{\Gamma_q} \boldsymbol{N}_p^{\mathrm{T}} \bar{\boldsymbol{q}} \, \mathrm{d}\Gamma - \boldsymbol{K}_{up}^{\mathrm{T}} \dot{\boldsymbol{u}}^h - \frac{1}{\gamma_f} \boldsymbol{H} \boldsymbol{p}^h - \boldsymbol{M} \dot{\boldsymbol{p}}^h \right). \tag{18l}$$

5. Total versus effective stress – one-element test

As mentioned above, Terzaghi's concept of effective stress $\boldsymbol{\sigma} = \boldsymbol{\sigma_t} + \boldsymbol{\Pi} p_f$ is used for the two-phase medium. The effective stress is responsible for the deformation and limit states of saturated soil. The balance of the medium is maintained by the total stress.

The numerical results for a one-element biaxial-compression test are presented in order to show the physical difference between the total and effective stresses. The following material data are adopted: Poisson's ratio $\nu = 0.2$, swelling index $\kappa = 0.013$, initial void ratio $e_0 = 0.1$, initial value of hardening parameter $p_{c0} = 0.25(4.0)\,\mathrm{MPa}$, compression index $\lambda = 0.032$, $M = 1.1$. The additional material data for the two-phase medium are: $\gamma_f = 10\,\mathrm{kN/m^3}$, bulk modulus for fluid $K_f = 10.0\,\mathrm{MPa}$ and permeability coefficient $k = 1.0\mathrm{e}{-}04\,\mathrm{m/day}$ (it does not influence the results in the considered case). The specimen dimensions are $1\,\mathrm{m} \times 1\,\mathrm{m}$. The boundary conditions are such that water cannot flow out of the sample ($\bar{\boldsymbol{q}} = \boldsymbol{0}$ on Γ). The calculations are carried out in two steps. The initial stresses

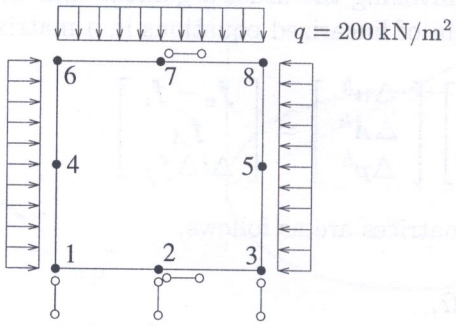

Fig. 2. Initial stress – static and kinematic boundary conditions

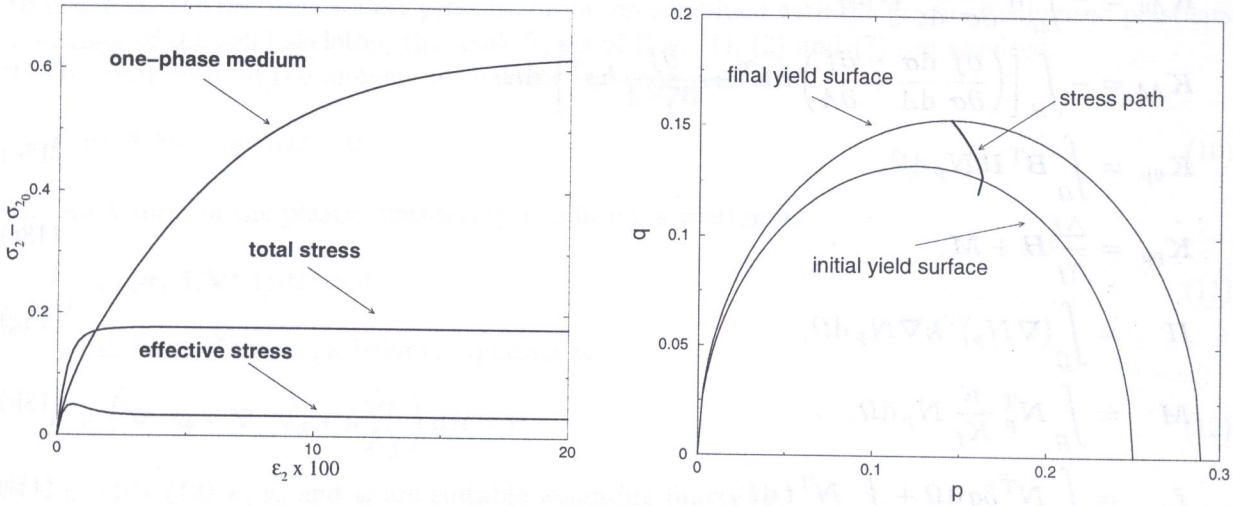

Fig. 3. One-element biaxial compression test, $p_{c0} = 0.25\,\mathrm{MPa}$; stress–strain diagrams for the vertical direction (left), yield surface evolution for two-phase medium (right)

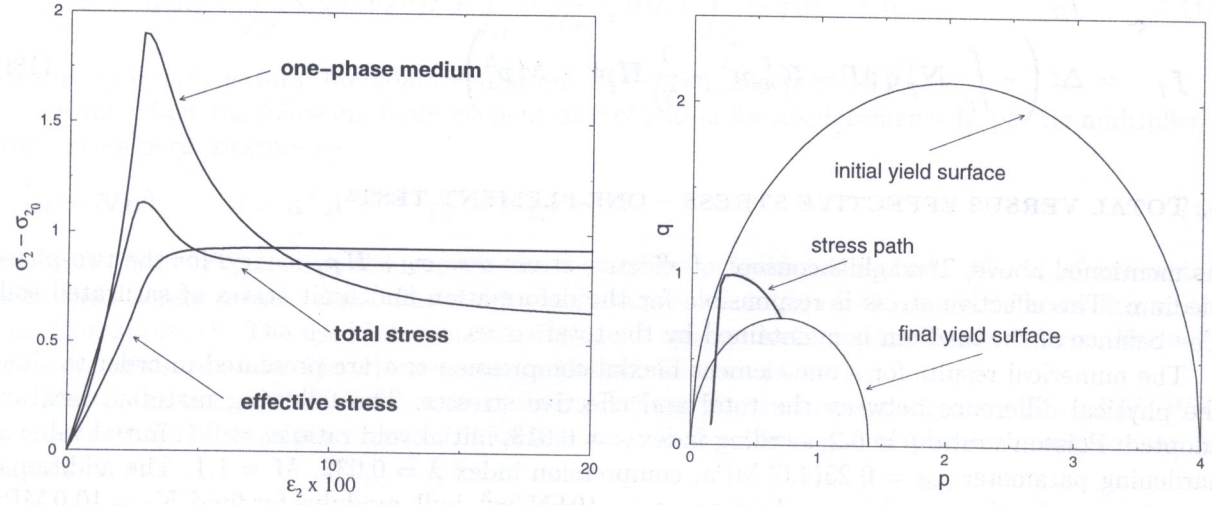

Fig. 4. One-element biaxial compression test, $p_{c0} = 4.0\,\mathrm{MPa}$; stress-strain diagrams for the vertical direction (left), yield surface evolution for two-phase medium (right)

$\boldsymbol{\sigma}_0 = [-0.2, -0.2, -0.08, 0.0]$ MPa are generated by a compressive traction as shown in Fig. 2. The initial excess pore pressure is equal to zero. In the second stage the compression process is driven under displacement control. The displacements of the nodes on the upper edge are prescribed to compress the sample.

In Figs 3–4 the stress–strain diagrams for one-phase soil under drained conditions ($p_f = 0$) and for undrained conditions in the two-phase medium are compared. They show a significant influence of the pore pressure on the results. The stress paths and yield surface evolution are also presented. Figure 3 shows the results for a contractant flow and Fig. 4 for a dilatant one. In both cases the yield surface and the critical state line is reached for smaller values of σ_2 for the undrained state. However, in Fig. 4 for $p_{c0} = 4.0$ MPa we can notice that the final value of σ_2 is higher for the undrained conditions. Moreover, in this case, the effective stress σ_2 is higher than the second component of the total stress vector. This effect is caused by the fact that the sign of p_f changes and the pore pressure becomes negative at a certain stage of the loading process.

6. Biaxial compression test

In order to verify the mesh sensitivity of the numerical solution the biaxial compression test is computed for a multi-element configuration. The size of the specimen is 1 m×2 m. It is discretized with 10×20, 20×40 and 40×80 finite elements. The following material data are adopted for the solid phase: $\nu = 0.2$, $\kappa = 0.013$, $e_0 = 1.0$, $p_{c0} = 2.0$ MPa, $\lambda = 0.032$, $M = 1.1$. For the fluid phase we take: $\gamma_f = 10\,\mathrm{kN/m^3}$, $K_f = 1.0e05$ kPa, $k = 1.0\mathrm{e}{-06}$ m/day.

The initial stresses $\boldsymbol{\sigma}_0 = [-0.2, -0.2, -0.08, 0.0]$ MPa are generated in a similar way as in the case of one-element test. The initial excess pore pressure is equal to zero. To load the sample a vertical traction (in the case of the local model) or displacements of the nodes (for gradient dependent Cam-clay) on the upper edge are prescribed to compress it. For the local model displacement control cannot be used due to a snap-back response and the linearized arc length control is employed. To initiate a shear band formation one element (four elements for the medium and sixteen for the fine mesh) in the bottom left-hand corner of the sample is assigned a 10% smaller value of the initial overconsolidation measure $p_{c0} = 1.8$ MPa.

The shear banding simulations for the local Cam-clay model (drained conditions) exhibit pathological mesh sensitivity and are presented in [18]. As expected, strains localize in the narrowest possible area determined by the element size.

6.1. Biaxial compression (two-phase local Cam-clay)

The purpose of the paper is to examine the influence of the fluid phase on instabilities in the Cam-clay soil model. Since, as mentioned in the Introduction, it is claimed that the fluid phase can introduce some regularization into the numerical model, the calculations are first carried out for a local (not regularized) Cam-clay model. At first, the boundary conditions are such that water cannot flow out of the sample (homogeneous natural boundary condition).

As can be seen in Figs. 5–7 the numerical results are not mesh-independent in this case and for the fine mesh the calculations were not completed due to convergence problems. Note that the contour plots for the second invariant of the strain tensor would look similarly to those of the vertical strain presented in Fig. 6. However, the pore pressure distribution shown in Fig. 7 does not exhibit localization in the narrowest zone, and in this respect is similar for all the three meshes. At the same time, in Fig. 5 a distinct snap-back is visible in the load-deformation curve (sometimes even two snap-backs are simulated). This fact and the problems with convergence during calculations suggest that in comparison to the one-phase medium (cf. results presented in [18]), the two phase material is less stable.

In order to avoid the numerical difficulties and snap-backs the calculations are then repeated for $p_{c0} = 1.0$ MPa ($p_{c0} = 0.9$ MPa for the imperfect region in the bottom left-hand corner of the

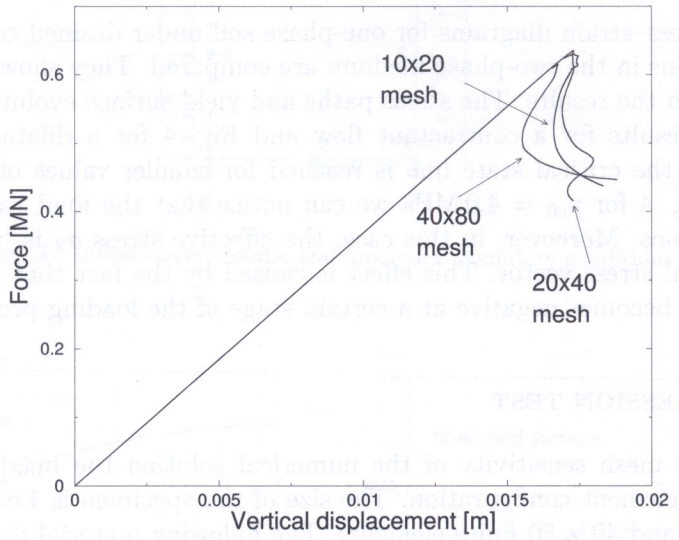

Fig. 5. Biaxial compression test for local Cam-clay model: load–deformation curves for $k = 1.0\text{e}{-}06\,\text{m/day}$

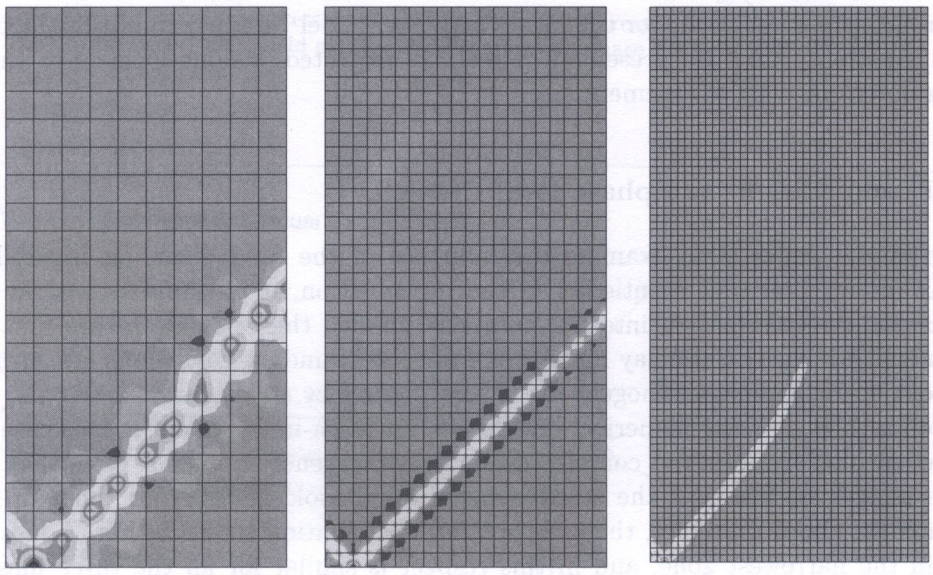

Fig. 6. Biaxial compression test for local Cam-clay model: vertical strain distribution for $k = 1.0\text{e}{-}06\,\text{m/day}$

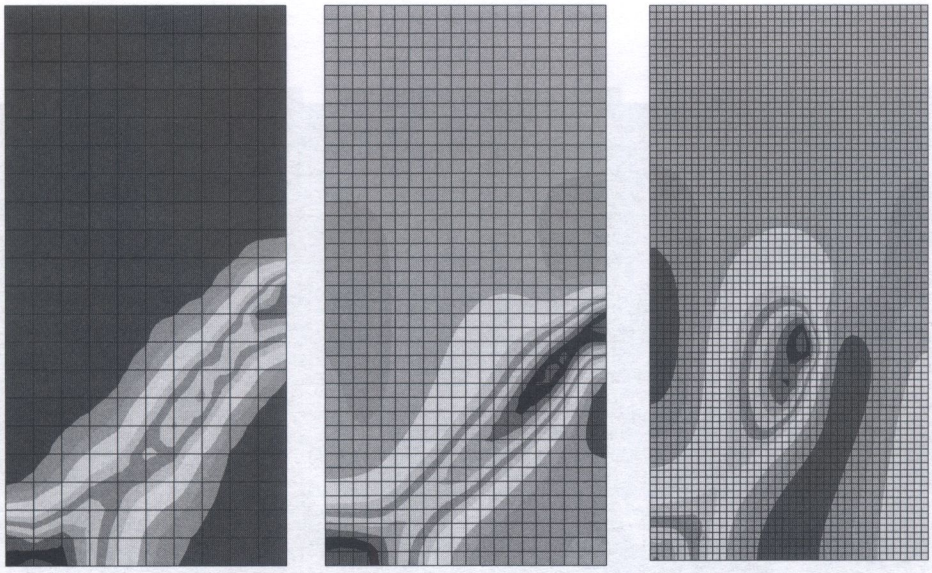

Fig. 7. Biaxial compression test for local Cam-clay model: pore pressure distribution for $k = 1.0\text{e}{-}06\,\text{m/day}$

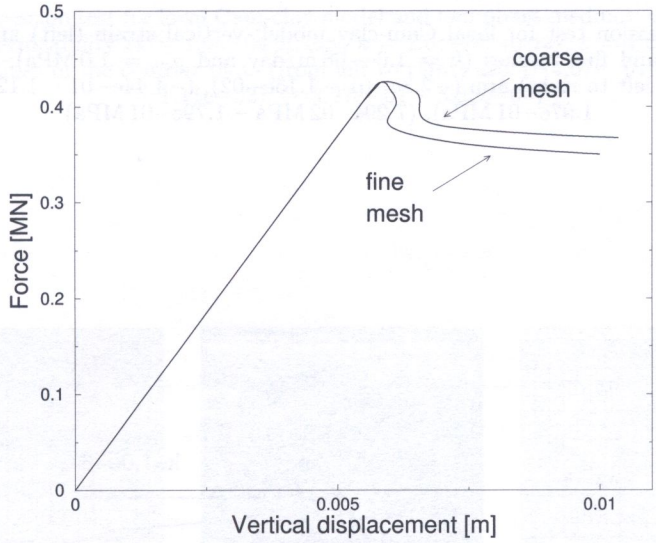

Fig. 8. Biaxial compression test for local Cam-clay model: load–deformation curves, coarse and fine meshes, $k = 1.0\text{e}{-}06\,\text{m/day}$ and $p_{c0} = 1.0\,\text{MPa}$

sample). The results for this data set (for two meshes) are presented in Figs. 8–9. The diagrams in Fig. 8 are different for coarse and fine meshes, vertical strain distribution (Fig. 9 left) shows the shear bands dependent on the adopted discretization, but the pore pressure distribution in Fig. 9 (right) seems to be nearly mesh-independent.

For one-phase medium with the same material data, both the local and gradient-dependent Cam-clay model exhibit very weak softening and the strain localization is almost invisible. Hence, the results of this example again lead to the conclusion that the fluid phase has a destabilizing influence. In order to examine the role of permeability coefficient k on the regularization effect of the fluid, the calculations for various values of k ($k = 1.0\text{e}{-}04\,\text{m/day}$, $k = 1.0\text{e}{-}06\,\text{m/day}$, $k = 1.0\text{e}{-}10\,\text{m/day}$) and for a permeable top edge have been performed. The selected results (for one mesh only) are presented in Figs. 10–12. The obtained contour plots for the vertical strain (Fig. 11) turned out to be mesh-dependent. Irrespectively of the value of k the strains localize in the narrowest possible area determined by the element size. On the other hand, the value of the

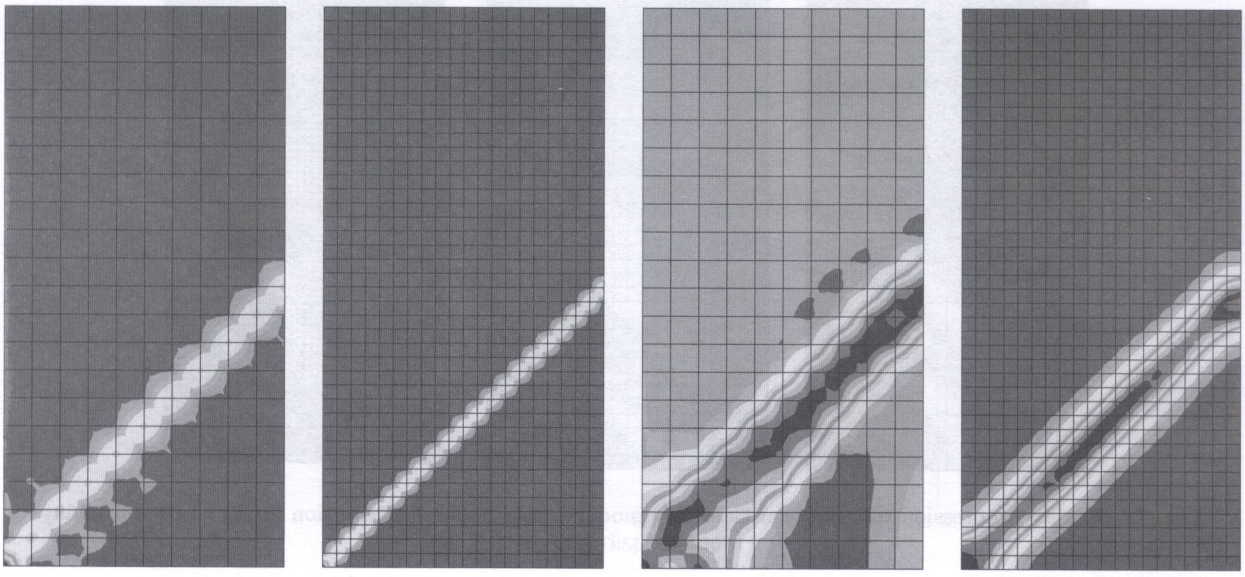

Fig. 9. Biaxial compression test for local Cam-clay model: vertical strain (left) and pore pressure (right) distribution for coarse and fine meshes (k = 1.0e−06 m/day and p_{c0} = 1.0 MPa); the ranges of values in the contour plots (from left to right) are: (−2.3e−01 – 1.15e−02), (−4.44e−01 – 1.12e−02), (6.5e−02 MPa – 1.97e−01 MPa), (7.29e−02 MPa – 1.79e−01 MPa)

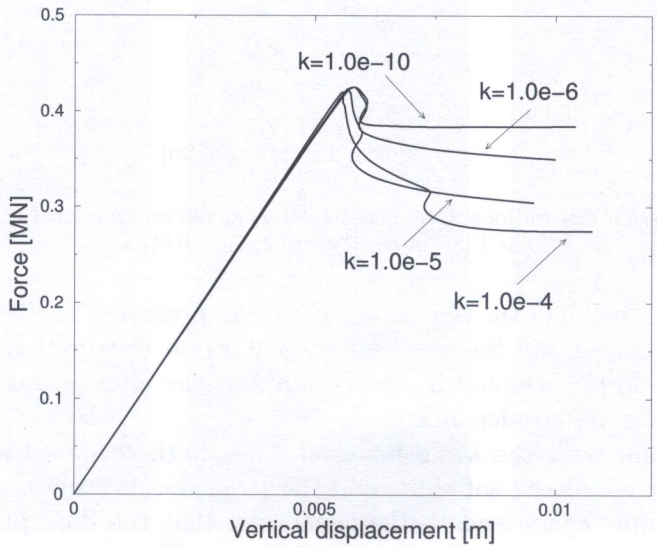

Fig. 10. Biaxial compression test for two-phase medium with local Cam-clay model: load–deformation curves for different values of permeability coefficient and permeable upper edge

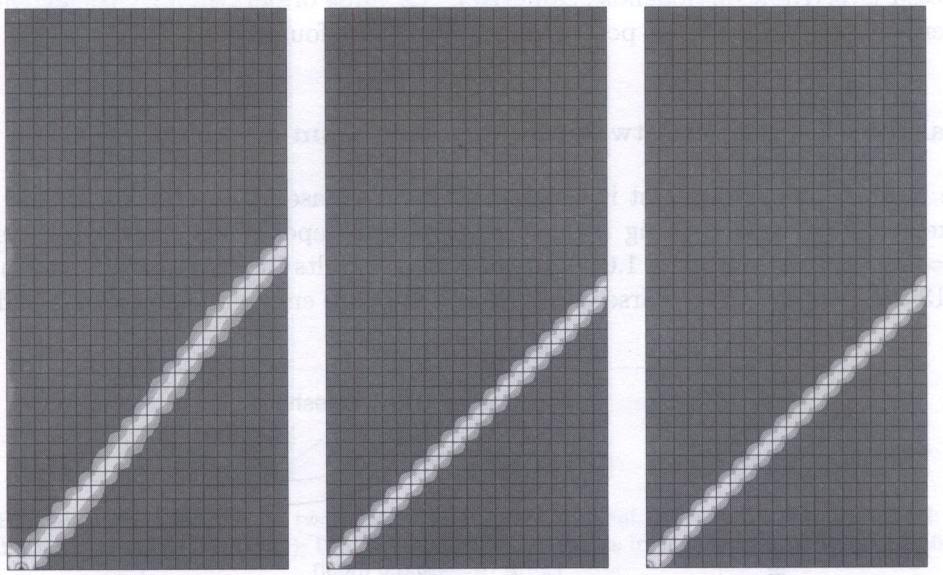

Fig. 11. Biaxial compression test for local Cam-clay model and two-phase medium: vertical strain distribution for various values of permeability (k = 1.0e−04 m/day, k = 1.0e−06 m/day, k = 1.0e−10 m/day, from left to right); the ranges of values in the contour plots (from left to right) are: (−4.67e−01 − 2.72e−02), (−4.46e−01 − 1.11e−02), (−3.97e−01 − 8.85e−04)

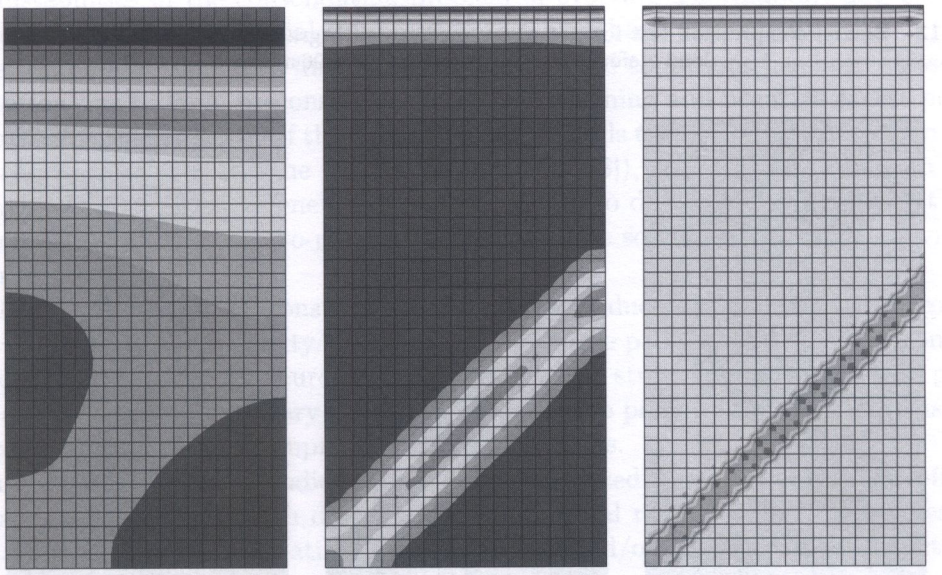

Fig. 12. Biaxial compression test for local Cam-clay model and two-phase medium: pore pressure distribution for various values of permeability (k = 1.0e−04 m/day, k = 1.0e−06 m/day, k = 1.0e−10 m/day, from left to right); the ranges of values in the contour plots (from left to right) are: (0.0 MPa − 1.18e−01 MPa), (0.0 MPa − 1.84e−01 MPa) (0.0 MPa − 2.77e−01 MPa)

permeability coefficient influences the direction of the localization band (cf. Fig. 11) and the critical load level for which the instability occurs (cf. Fig. 10). Moreover, for the case of permeable top edge, the pore pressure distribution depends strongly on the value of permeability coefficient, cf. Fig. 12. For large permeability no localized pore pressure pattern is found.

6.2. Biaxial compression test (two-phase gradient Cam-clay model)

Finally, the biaxial compression test is computed for two-phase medium in which the behaviour of the solid skeleton is described using regularized, gradient-dependent Cam-clay model with $p_{c0} = 2.0\,\mathrm{MPa}$, $c = 0.05\,\mathrm{kN^2/m^2}$ and $k = 1.0\mathrm{e}{-}06\,\mathrm{m/day}$. The results for this case are shown in Figs. 13–15. In Fig. 13 the results for the coarse mesh are not accurate enough due to standard discretization

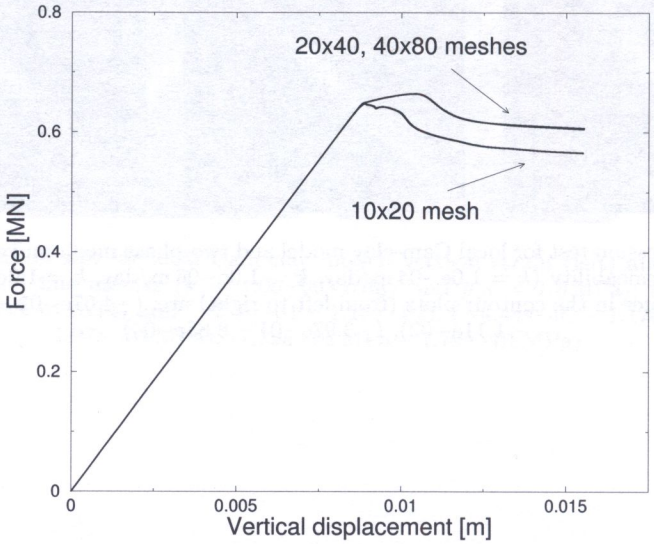

Fig. 13. Biaxial compression test for two-phase medium with gradient-dependent Cam-clay model: load–deformation curves ($k = 1.0\mathrm{e}{-}06\,\mathrm{m/day}$)

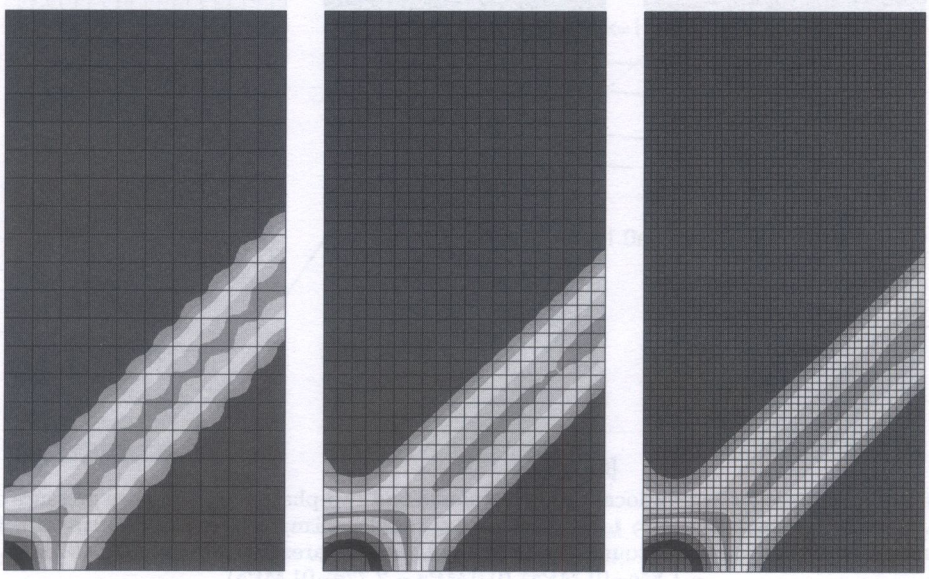

Fig. 14. Biaxial compression test for two-phase medium with gradient-dependent Cam-clay model: vertical strain distribution ($k = 1.0\mathrm{e}{-}06\,\mathrm{m/day}$); the (average) range of values in the contour plots is ($-5.4\mathrm{e}{-}02$ – $-8.65\mathrm{e}{-}03$)

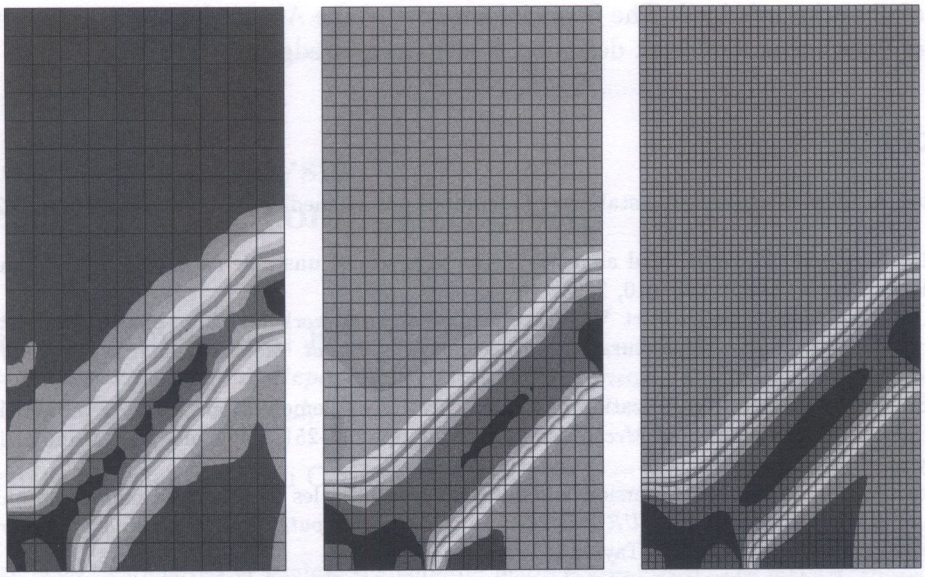

Fig. 15. Biaxial compression test for two-phase medium with gradient-dependent Cam-clay model: pore pressure distribution (k = 1.0e−06 m/day); the (average) range of values in the contour plots is (−8.56e−03 MPa − 3.04e−01 MPa)

error. However, the diagrams for the medium and fine mesh coincide. The strain and pore pressure distributions in Figs. 14–15 are also mesh independent.

7. Conclusions

In the paper a two-phase gradient-dependent soil model which is an extension of the modified Cam-clay plasticity formulation has been derived. A three field finite element has been proposed for the analysis of instabilities in the consolidation problem of evolving deformations and pore pressures. A set of computations for the biaxial compression test have been performed.

First, the response of the model for drained and undrained conditions has been assessed. For the case of dilatation due to large preconsolidation, strong softening and negative excess pore pressure have been predicted. The analysis of the numerical results leads to the conclusion that, in comparison to a one-phase material (cf. also the results presented in [18]), the two-phase medium has a lower load-carrying capacity and is in general less stable. Thus, no distinct stabilizing effect of the fluid phase has been observed in the two-phase medium with the soil skeleton described with the local Cam-clay model.

The (inelastic) strain distributions obtained for various values of the permeability coefficient are sensitive to the discretization density. On the other hand, the pore pressure distributions are nearly mesh-independent. The pore pressure distribution depends strongly on the value of permeability coefficient (and also on the boundary conditions for the pore pressure field). It remains to examine the influence of the fluid phase compressibility on the results.

The results obtained for the gradient-enhanced (regularized) theory and the three-field element do not show the pathological mesh dependence of numerical result due to instabilities and strain localization. Therefore, a regularization of the softening and/or nonassociative constitutive model for soil is mandatory also within a two-phase description.

Acknowledgments

Paper based on research carried out within grant PB 8 T07A 006 20 of the Polish Committee for Scientific Research. Valuable discussions with Prof. Andrzej Truty from Cracow University of Technol-

ogy are gratefully acknowledged. The financial support of the Alexander von Humboldt Foundation in the form of equipment and book donation is also acknowledged.

References

[1] J.P. Bardet, A. Shiv. Plane-strain instability of saturated porous media. *ASCE J. Eng. Mech.*, **121**(6): 717–724, 1995.

[2] A. Benallal, C. Comi. On numerical analyses in the presence of unstable saturated porous materials. *Int. J. Numer. Meth. Engrg.*, **56**(6): 883–910, 2003.

[3] R. Borja. Cam-Clay plasticity. Part V: A mathematical framework for three-phase deformation and strain localization analyses of partially saturated porous media. *Comput. Methods Appl. Mech. Engrg.*, **193**: 5301–5338, 2004.

[4] V.D. da Silva. Viscoplastic regularization of a Cam-clay FE-implementation. In W. Wunderlich, editor, *Proc. European Conf. on Computational Mechanics ECCM'99*, pp. 250–251, paper no. 422, Munich, 1999. Technical University of Munich.

[5] R. de Borst, M.-A. Abellan. Dispersion and internal length scales in strain-softening two-phase media. In G. Meschke et al., editors, *Proc. EURO-C 2006 Int. Conf. Computational Modelling of Concrete Structures*, pp. 549–556, London/Leiden, 2006. Taylor & Francis.

[6] R. de Borst, H.-B. Mühlhaus. Gradient-dependent plasticity: Formulation and algorithmic aspects. *Int. J. Numer. Meth. Engrg.*, **35**: 521–539, 1992.

[7] R. de Borst, J. Pamin. Some novel developments in finite element procedures for gradient-dependent plasticity. *Int. J. Numer. Meth. Engrg.*, **39**: 2477–2505, 1996.

[8] A. Gens, D.M. Potts. Critical state models in computational geomechanics. *Eng. Comput.*, **5**: 178–197, 1988.

[9] A. Groen. *Three-dimensional elasto-plastic analysis of soils.* Ph.D. dissertation, Delft University of Technology, Delft, 1997.

[10] J. Larsson. *On the modeling of porous media with emphasis on localization.* Ph.D. dissertation, Chalmers University of Technology, Gothenburg, 1999.

[11] X. Liu, A. Scarpas, J. Blaauwendraad. Numerical modelling of nonlinear response of soil. Part 2: Strain localization investigation on sand. *Int. J. Solids Struct.*, **42**: 1883–1907, 2005.

[12] H.-B. Mühlhaus, E.C. Aifantis. A variational principle for gradient plasticity. *Int. J. Solids Struct.*, **28**: 845–857, 1991.

[13] F. Oka, Y. Higo, S. Kimoto. Effect of dilatancy on the strain localization of water-saturated elasto-viscoplastic soil. *Int. J. Solids Struct.*, **39**: 3625–3647, 2002.

[14] M. Ortiz, A. Pandolfi. A variational Cam-clay theory of plasticity. *Comput. Methods Appl. Mech. Engrg.*, **193**: 2645–2666, 2004.

[15] P.M. Pinsky. A finite element formulation for elastoplasticity based on three-field variational equation. *Comput. Methods Appl. Mech. Engrg.*, **61**: 41–60, 1987.

[16] K.H. Roscoe, J.B. Burland. On the generalized behaviour of 'wet' clay. In *Engineering Plasticity*, volume 48, pages 535–609, Cambridge, 1968. Cambridge University Press.

[17] B.A. Schrefler, L. Sanavia, C.E. Majorana. A multiphase medium model for localisation and postlocalisation simulation in geomechanics. *Mech. Cohes.-frict. Mater.*, **1**: 95–114, 1996.

[18] A. Stankiewicz, J. Pamin. Gradient-enhanced cam-clay model in simulation of strain localization in soil. *Foundations of Civil and Environmental Engineering*, **7**: 293–318, 2006.

[19] A. Truty. On certain class of mixed and stabilized mixed finite element formulations for single and two-phase geomaterials. Monograph 48, Cracow University of Technology, Cracow, 2002.

[20] H.W. Zhang, B.A. Schrefler. Gradient-dependent plasticity model and dynamic strain localisation analysis of saturated and partially saturated porous media: one dimensional model. *Eur. J. Mech. A/Solids*, **19**(3): 503–524, 2000.

[21] H.W. Zhang, B.A. Schrefler. Particular aspects of internal length scales in strain localisation analysis of multiphase porous materials. *Comput. Methods Appl. Mech. Engrg.*, **193**: 2867–2884, 2004.

[22] O.C. Zienkiewicz, A.H.C. Chan, M. Pastor, B.A. Schrefler, T. Shiomi. *Computational Geomechanics.* John Wiley & Sons, Chichester, 2000.